

Fast Fourier Transform-weighted Photoacoustic Imaging by in vivo Magnetic Alignment of Hybrid Nanorods

Zhiwei Li^{†#}, Zhouqi Meng^{†#}, Feng Tian^{†§}, Zuyang Ye[†], Xuanfang Zhou[‡], Xingjian Zhong[§], Qian Chen[‡], Mo Yang[§], Zhuang Liu^{‡}, and Yadong Yin^{*†}*

[†]Department of Chemistry, University of California, Riverside, CA 92521, USA.

[‡]Institute of Functional Nano & Soft Materials (FUNSOM), Jiangsu Key Laboratory for Carbon-Based Functional Materials & Devices, Soochow University, Suzhou, Jiangsu 215123, China

[§]Department of Biomedical Engineering, The Hong Kong Polytechnic University, Hung Hom, Kowloon, Hong Kong, China

*Correspondence: yadong.yin@ucr.edu, zliu@suda.edu.cn

[#]These authors contributed equally to this work.

ABSTRACT: Photoacoustic (PA) imaging uses photon-phonon conversion for high-resolution tomography of biological tissues and functions. Exogenous contrast agents are often added to improve the image quality, but the interference from endogenous molecules diminishes the imaging sensitivity and specificity. We report a background-free PA imaging technique based on the active modulation of PA signals via magnetic alignment of Fe₃O₄@Au hybrid nanorods. Switching the field direction creates enhanced and deactivated PA imaging modalities, enabling a simple pixel subtraction to effectively minimize background noises. Under an alternating

magnetic field, the nanorods exhibit PA signals of coherently periodic changes that can be converted into a sharp peak in a frequency domain via the fast Fourier transform. Automatic pixel-wise screening of nanorod signals performed using a computational algorithm across a time-sequence set of PA images regenerates a background-free PA image with significantly improved contrast, specificity, and fidelity.

KEYWORDS: Photoacoustic imaging, Fe₃O₄@Au nanorods, background-free imaging, FFT imaging processing, magnetic alignment, plasmonic nanostructures

Photoacoustic (PA) imaging utilizes the photoacoustic effect of a contrast agent for multiscale imaging of biological structures and functions.¹⁻⁴ Because the scattering of ultrasonic waves in biological tissue is three orders of magnitude smaller than photons, PA imaging features deeper tissue penetration and finer *in vivo* spatial resolution than optical imaging techniques.⁵⁻⁷ Some endogenous molecules, such as hemoglobin and melanin, can generate PA signals to visualize tissue structures and functions.^{8,9} In most cases, exogenous contrast agents are necessary to improve the imaging contrast in specific targets, like solid tumors.¹⁰⁻¹² While various PA probes, including dye molecules,¹³ plasmonic nanostructures,^{14, 15} carbon materials,¹⁶⁻¹⁸ and organic particles¹⁹⁻²¹ exhibit improved contrast in the targeted tissues, minimizing background signals from the endogenous molecules remains challenging in conventional PA images.⁹ These noises interfere with probe signals and reduce the imaging specificity and resolution. Background-free PA tomography can overcome this long-lasting challenge by dynamically modulating the PA signals through external stimuli, such as magnetic field,²² heat,²³ ultrasound,²⁴⁻²⁶ and light.²⁷ For example, ultrasound-sensitive microbubbles have been used for *in vivo* background-free PA imaging based on their responsive PA signals and pixel subtraction method.²⁵ Photoswitching upconversion nanoparticles have also been developed for super-sensitive PA molecular imaging, which could reliably remove PA noises and enhance imaging sensitivity.²⁷ However, it remains challenging to use a

simple pixel subtraction algorithm to completely remove the noises in the reconstructed images because they randomly fluctuate in the biological tissues. Pixel subtraction also means a simultaneous decay in PA signals from contrast agents, leading to undesirable decreases in signal-to-noise ratio. Therefore, developing stimuli-responsive PA probes and new data processing methods are highly desirable in advancing background-free imaging techniques.

An ideal active PA contrast agent for cancer diagnosis should have a high absorption coefficient for efficient PA conversion, good biocompatibility, and reversible and instant responses to external stimuli.²⁸ The application of an external stimulus should be compatible with the noninvasive imaging modalities without sacrificing the advantages of PA imaging. Herein, we report a magnetically modulated, fast Fourier transform (FFT)-weighted PA imaging platform using Fe₃O₄@Au hybrid nanorods (NRs) as an active contrast agent. Such nanorods are produced using a space-free confined growth strategy by growing a layer of Au with a controllable thickness at the hard-soft interface of Fe₃O₄@polymer core-shell nanorods. Applying a magnetic field during PA imaging aligns the nanorods *in vivo*. Changing the field direction can further enable reversible tuning of nanorods' plasmonic excitation, photothermal conversion, and photoacoustic effect. Using these nanorods as active contrast agents, we first demonstrate a magnetically modulated background-free PA imaging technique using a pixel-subtraction method. Normal PA images can be acquired without a magnetic field after the administration of Fe₃O₄@Au NRs (step i in **Figure 1a**). Under a perpendicular magnetic field relative to incident light, Fe₃O₄@Au NRs are aligned parallel to the field, and an enhanced PA mode is created due to full excitation of the longitudinal plasmon resonance (step ii in **Figure 1a**). Switching the magnetic field to a parallel direction suppresses the longitudinal plasmon, generating a deactivated PA mode (step iii in **Figure 1a**). Subtracting pixels of deactivated mode from those of enhanced mode can largely remove random PA noises, creating background-free PA images (step iv in **Figure 1a**). To completely remove any static or random PA backgrounds, we further develop an FFT-weighted imaging technique by simultaneously performing PA imaging under an alternating magnetic field (**Figure 1b**). A series of PA images in time domains are

acquired, and the PA intensity of each pixel from this image sequence is extracted (steps i and ii in **Figure 1c**). Then, the time-domain signals are converted into frequency-domain signals by FFT so that the periodic rod signals can be readily recognized as sharp peaks and distinguished from static and random noises (step iii in **Figure 1c**). Finally, a background-free PA image can be created by recovering signals from the frequency-domain peak intensity, leading to the complete removal of noises and greatly enhanced sensitivity and specificity (Step iv in **Figure 1c**).

To optimize photoacoustic performance, we calculate the optical cross-sections of Au nanoshells templated against 110-nm Fe₃O₄ NRs. **Figure S1a** reveals the tuning of the longitudinal peak from NIR-II to NIR-I by increasing nanoshell thickness. Our simulation results demonstrate an ideal nanoshell thickness of ~10 nm, with the strongest absorption at 1030 nm (**Figure S1b**). Experimentally, the space-free confined growth of Au nanoshells follows the procedure in **Figure S2a**. As shown in the transmission electron microscopy (TEM) in **Figure S2b**, FeOOH nanorods (20 nm×110 nm) were first synthesized via a hydrothermal process and then converted into Fe₃O₄ NRs through surface-protected reduction.²⁹ The Fe₃O₄ NRs are superparamagnetic due to their polycrystallinity, small domain size, and low blocking temperature.^{29, 30} The nanorod surface was modified by cystamine through Fe-amino coordination and then immobilized with 2-nm Au seeds through Au-S coordination¹⁵ (**Figure S2c**). Unrestrained seeded growth produced Au clusters with grain sizes larger than 10 nm (**Figure S3**) and thick Au shells with scattering-dominated optical properties.^{15, 31} The synthetic challenge of thin Au nanoshells could be overcome by limiting the free Au growth along radial directions through a deformable resorcinol-formaldehyde (RF) phenolic resin, which was introduced after attaching Au seeds. The high permeability of the phenolic shell allows fast mass transfer for successive seeded growth, while its deformability limits the growth along radial directions and promotes the lateral Au growth into a thin nanoshell.

Seeded growth requires exquisite control over reaction kinetics to minimize self-nucleation, which has been explored using coordinating molecules to decrease the reduction potential of metal precursors.^{32, 33}

These methods typically produced isolated, large Au particles (**Figure S4**) due to Ostwald ripening.³⁴ In this work, we introduce H₂O₂ as a weak reducing agent to lower the reduction rate of Au precursors and avoid the undesirable seed ripening and self-nucleation (**Figure S5**).³⁵ The plasmon coupling between neighboring Au domains induces broad-band absorption (extinction spectrum at 2.5 min in **Figure S6**). Because the RF shells limit the radial Au deposition, we observed elongated growth of Au nanostructures alongside the hard-soft interfaces and the fusion of neighboring grains into conformal Au coating (**Figure 2a**). The high-angle annular dark-field (HAADF) and elemental mapping images in **Figure 2b** show the concentric 10-nm Au coating on Fe₃O₄ nanorods. The interfacial growth is further confirmed by the gradual appearance of the plasmon band at a long wavelength (**Figure S6**), which blueshifts to 1030 nm due to the formation of complete Au nanoshells. The RF shells can be etched away by NaOH at 80°C (**Figure S7**). Due to the decreased refractive index from 1.65 of RF to 1.333 of water, we observed a 50-nm blueshift of the transverse and longitudinal bands and a simultaneous solution color change from green to red (**Figure 2c**). We tested the photostability of the nanorods under 980-nm laser irradiation at 1.2 W. The spectra in **Figure S8** showed negligible changes in peak position and intensity, demonstrating good stability of the hybrid nanorods. To evaluate the photothermal property, we measured the heating curve of the Fe₃O₄@Au nanorod solution using a 980-nm laser (**Figure S9a**), which shows an increase of temperature to 45.1°C, with the extinction of 1.886 at 980 nm (**Figure S9b**). By manipulating the temperature change during cooling in the heating curve (**Figure S9c**), we estimated the photothermal conversion efficiency at 46.83%. Compared with Au nanorods, the Au nanoshells have a higher photothermal conversion efficiency mainly because of their high absorbance/scattering ratio.³⁶

We first consider a theoretical model to understand the orientation-dependent plasmonic excitation of Au nanoshells (**Figure S10a**). The calculated spectra exhibit a 930-nm peak when the field direction is parallel ($|0^\circ\rangle$) and a 530-nm peak when perpendicular ($|90^\circ\rangle$) to light polarization (**Figure S10b**), suggesting the selective excitation of longitudinal and transverse modes. Quantitative analysis suggests a \cos^2 - and \sin^2 -function for the longitudinal and transverse plasmonic excitation (**Figure 2d**).

Experimentally, such preferential alignment is enabled by the unique magnetic anisotropy of Fe₃O₄ NRs, which drives their parallel alignment to the field direction to minimize the magnetic potential energy.³⁷⁻⁴¹ As shown in **Figure 2e**, the longitudinal peak at 930 nm is maximized when the field is oriented at |0°> or deactivated at |90°>. An inverse trend is observed on the transverse plasmon band. The electric field distributions in **Figure 2f** indicate a dipole resonance of Au nanoshells in the two modes. These optical observations are consistent with the theoretical considerations, demonstrating the responsive and integrated properties of Fe₃O₄@Au NRs. As the acoustic signals are the thermal fluctuation-induced pressure waves, their active modulation requires dynamic regulation of the photothermal conversion of the contrast agent. Therefore, we examined the photothermal properties of Fe₃O₄@Au NRs under different magnetic fields. As shown in **Figure 2g**, the temperature increased to ~48°C when the magnetic field was parallel (|0°>) to the light polarization. The thermal conversion was significantly suppressed under a perpendicular field (|90°>), leading to a much smaller temperature increase. The maximum longitudinal excitation of Au shells at |0°> corresponds to the highest temperature increases in the colloidal dispersion under 980-nm laser irradiation (**Figure 2h**). The extinction intensity of the nanorod dispersion at the resonant wavelength shows periodic, coherent changes under an alternating magnetic field with a frequency of up to 3 Hz (**Figure S11a**). If the periodic signals in the time domain are converted into intensity in the frequency domain by FFT (**Figure 2i**), the FFT frequency is exactly twice the applied frequency with a linear fitting coefficient of R²=0.99913. The signal maintains coherent oscillation without any noticeable decay and maladjustment, demonstrating good colloidal stability and performance consistency of Fe₃O₄@Au NRs (**Figure S11b**).

We measured the photoacoustic absorption spectra of AuNRs and Fe₃O₄@Au NRs to study their photoacoustic responses under magnetic fields. In **Figure S12a**, the spectra of AuNRs show negligible intensity changes in the absence and presence of magnetic fields. In the case of Fe₃O₄@Au NRs, the absorption intensity can be reversibly and remotely modulated multiple times using a magnetic field (**Figure S12b**). In acquiring PA images in an alternating magnetic field, AuNRs only produce fluctuated

PA signals without noticeable magnetic responses (**Figures 3a** and **3b**), while $\text{Fe}_3\text{O}_4@\text{Au}$ NRs exhibited reversible PA signal changes. Their PA signals showed twofold enhancement when the magnetic field was switched from parallel to perpendicular to light incidence (**Figure 3c**). These observations are consistent with the orientation-dependent optical extinction and photothermal conversion, appreciating the magnetic orientational control of nanorods for noninvasive, precise, instant, and reversible tuning of the PA signals. The background-free imaging was firstly performed using polydopamine (PDA) phantoms with different PDA concentrations. The PA signals of AuNRs in **Figure 3d** were not responsive under different PDA concentrations in the phantoms, while the signals of $\text{Fe}_3\text{O}_4@\text{Au}$ NRs were enhanced by changing a parallel magnetic field to a perpendicular one (**Figure 3e**). Therefore, both the noises and non-responsive AuNRs signals were removed after pixel subtraction (**Figure 3f**). In **Figure 3g**, however, the PDA noises of varying intensities were removed, and the signals from the $\text{Fe}_3\text{O}_4@\text{Au}$ NRs remained in the injected regions after pixel subtraction.

For *in vivo* imaging, we first evaluated the biocompatibility of the nanorods by culturing them with cells for 24 hours. As shown in **Figure S13**, the cell viability has negligible changes, demonstrating good biocompatibility and low toxicity of the nanorods. We started with a mouse muscle model by stereotaxic injection of AuNRs and $\text{Fe}_3\text{O}_4@\text{Au}$ NRs into two separate regions (**Figure 4a**). As expected, the PA signals from AuNRs did not respond to external magnetic fields (upper panel in **Figure 4b**) and were eliminated after pixel subtraction. In mice injected with $\text{Fe}_3\text{O}_4@\text{Au}$ NRs (middle panel in **Figure 4b**), the PA signals were highly tunable by switching the magnetic field direction, making it possible to subtract the pixels of the deactivated mode from that of the enhanced mode. If AuNRs and $\text{Fe}_3\text{O}_4@\text{Au}$ NRs were separately injected into a mouse's left and right sides (bottom panel in **Figure 4b**), the PA signal of $\text{Fe}_3\text{O}_4@\text{Au}$ rods exhibited significant enhancement while that of AuNRs only randomly fluctuates, with the noises from AuNRs being completely removed by pixel-wise subtraction. The resulting differential image, overlapped with acoustic anatomical reference, revealed specific background-free contrast from the muscle region injected with $\text{Fe}_3\text{O}_4@\text{Au}$ NRs (**Figure 4c**). The background-free imaging was further

performed on a subcutaneous tumor model in mice. The blood vessels were first treated with erlotinib to enhance the tumor penetration of $\text{Fe}_3\text{O}_4@\text{Au}$ NRs.⁴² The sharper and stronger fluorescence in erlotinib-treated groups demonstrated their enhanced permeability of the blood vessels compared with untreated groups (**Figure S14**). $\text{Fe}_3\text{O}_4@\text{Au}$ NRs were then intravenously (i.v.) injected and targeted to the tumor via the enhanced permeability and retention (EPR) effect (**Figure 4d**). During PA imaging, an external magnetic field was applied to align the $\text{Fe}_3\text{O}_4@\text{Au}$ NRs in the tumor site. Again, dynamic signal changes were observed in mice injected with $\text{Fe}_3\text{O}_4@\text{Au}$ NRs (bottom panels in **Figure 4e**) but not those with AuNRs (upper panels in **Figure 4e**), creating background-free contrast in the imaging areas upon pixel subtraction. The average PA signal of background-free imaging in the tumor injected with AuNRs (**Figure 4f**) or in the one only treated with $\text{Fe}_3\text{O}_4@\text{Au}$ NRs (**Figure 4g**) is ~ 10 times lower than that treated with $\text{Fe}_3\text{O}_4@\text{Au}$ NRs and erlotinib (**Figure 4h**), demonstrating the successful regulation of PA signals and the removal of PA noises from the endogenous sources.

Endogenous PA noises can vary in a broad range in intensity, distribution, and depth.⁴³⁻⁴⁵ While pixel subtraction can largely overcome this challenge, it still has its limit when noises and their temporal fluctuation are so strong that data processing is unresolvable. To further improve the image quality, we propose a magnetically modulated, FFT-weighted background-free PA imaging technique using periodic PA signals of $\text{Fe}_3\text{O}_4@\text{Au}$ NRs under an alternating magnetic field (**Figure 5a**). In the acquired PA images within a properly chosen time sequence, the signal changes of each pixel in PA images are extracted and plotted in real time. In the time domain, Au nanoshell signals feature periodic changes, while the background noise pixel shows random fluctuations. FFT is then applied to convert these time-domain signals to frequency-domain intensity. In principle, only periodic signals generate sharp peaks at a resonant frequency, while the random PA noises do not feature any peaks in the frequency domain. As a result, FFT-weighted PA images can thus be created using peak intensity in the frequency domain. This pixel-wise data processing was carried out using a programmed code in Matlab, with time-sequence PA

images as input and FFT-weighted PA images as output (See Supplementary Information for the program code).

We first tested the reversible tuning of PA signals *in vivo*. PA intensity from non-responsive AuNRs remained random (**Figure 5b**) under different magnetic fields due to the lack of magnetic response. In tumors administrated with Fe₃O₄@Au NRs, PA signals can be reversibly and quickly modulated by applying an alternating magnetic field (**Figures 5c, S15 and S16**). The time-dependent PA intensity of two pixels from tumor and background in **Figure 5d** exhibited periodic signal changes in tumor and random fluctuation, respectively. Such periodic signals from the Fe₃O₄@Au NRs could be readily recognized and distinguished from biological noises by FFT, with a single, sharp peak at ~0.25 Hz in the frequency domain (**Figure 5e**). After the pixel-wise screening of periodic signals, an FFT-weighted PA image was created based on the FFT intensity in the frequency domain. Compared with conventional PA modes (**Figure 5f**), the FFT-weighted PA image shows greatly reduced biological or electronic noises and highly specific PA signals from the active contrast agents (**Figures 5g**), demonstrating a seventeen-time enhancement in the signal-to-noise ratio (**Figures 5h and S17**). This imaging technique analyzes the PA signal frequency rather than intensity, making it less susceptible to randomly fluctuating noises than the pixel-wise subtraction method.

In summary, we report a magnetically modulated, FFT-weighted PA imaging technique using Fe₃O₄@Au nanorods as active contrast agents. Enabled by the interfacial seeded growth method, the hybrid nanorods exhibit integrated plasmonic and magnetic properties, allowing their photoacoustic properties to be instantaneously, remotely, and reversibly tuned by magnetic fields. In the muscle and tumor models, we have demonstrated highly tunable PA signals using *in vivo* nanoscale magnetic orientational control, leading to deactivated and enhanced PA modes. The new FFT-weighted imaging technique converts the coherent PA signal oscillation of Fe₃O₄@Au NRs under an alternating magnetic field to frequency-domain intensity, which is then used to create PA images against a frequency threshold to remove random noise signals. Compared with existing background-free PA imaging, the FFT-weighted imaging technique

removes both static and random noises and creates improved PA images. Because applying a magnetic field is simple and highly compatible with the conventional PA imaging process, the methodology developed in this work holds the potential to build an advanced background-free PA imaging platform for clinical applications.

ASSOCIATED CONTENT

Supporting Information

Experimental details, TEM images, extinction spectra, simulation results, photoacoustic absorption spectra, confocal fluorescence images, PA images, and Matlab codes for FFT data processing, including Figures S1-S15 (PDF).

AUTHOR INFORMATION

Corresponding Author

*E-mail: yadong.yin@ucr.edu

*E-mail: zliu@suda.edu.cn

ORCID

Zhiwei Li: 0000-0002-1489-4506

Yadong Yin: 0000-0003-0218-3042

Author Contributions

Z. Li, Z. Liu, and Y. Yin designed the concept and experiments. Z. Li synthesized and characterized the materials. Z. Li, Z. Meng, F. Tian, X. Zhou, X. Zhong, and Q. Chen carried out the PA imaging and

analysis. M. Yang contributed analysis tools. All the authors were involved in the data analysis. Z. Li wrote the manuscript with the help of all the co-authors. Y. Yin and Z. Liu revised the manuscript.

Notes

The authors declare no competing financial interest.

ACKNOWLEDGMENT

This work was supported by the U.S. National Science Foundation (CHE-1808788). Z. Liu acknowledges the support from the National Natural Science Foundation of China (21927803), a Collaborative Innovation Center of Suzhou Nano Science and Technology, and a '111' program from the Ministry of Education of China. The authors thank Yin Xiao and Wen Chen in the department of electronic and information engineering at the Hong Kong Polytechnic University for help in programming the code for data processing. The authors also thank the Central Facility for Advanced Microscopy and Microanalysis at UCR for help with TEM analysis.

REFERENCES

1. Wang, L. V.; Hu, S. Photoacoustic tomography: in vivo imaging from organelles to organs. *Science* **2012**, 335, (6075), 1458-1462.
2. Knox, H. J.; Chan, J. Acoustogenic Probes: A New Frontier in Photoacoustic Imaging. *Acc. Chem. Res.* **2018**, 51, (11), 2897-2905.
3. Fu, Q.; Zhu, R.; Song, J.; Yang, H.; Chen, X. Photoacoustic imaging: contrast agents and their biomedical applications. *Adv. Mater.* **2019**, 31, (6), 1805875.
4. Omar, M.; Aguirre, J.; Ntziachristos, V. Photoacoustic mesoscopy for biomedicine. *Nat. Biomed. Eng.* **2019**, 3, (5), 354-370.
5. Wang, L. V. Multiscale photoacoustic microscopy and computed tomography. *Nat. Photonics* **2009**, 3, (9), 503-509.
6. Hai, P.; Imai, T.; Xu, S.; Zhang, R.; Aft, R. L.; Zou, J.; Wang, L. V. High-throughput, label-free, single-cell photoacoustic microscopy of intratumoral metabolic heterogeneity. *Nat. Biomed. Eng.* **2019**, 3, (5), 381-391.
7. Na, S.; Russin, J. J.; Lin, L.; Yuan, X.; Hu, P.; Jann, K. B.; Yan, L.; Maslov, K.; Shi, J.; Wang, D. J. Massively parallel functional photoacoustic computed tomography of the human brain. *Nat. Biomed. Eng.* **2021**, 1-9.
8. Xu, M.; Wang, L. V. Photoacoustic imaging in biomedicine. *Rev. Sci. Instrum.* **2006**, 77, (4), 041101.

9. Weber, J.; Beard, P. C.; Bohndiek, S. E. Contrast agents for molecular photoacoustic imaging. *Nat. Meth.* **2016**, *13*, (8), 639-650.
10. Xia, Y.; Li, W.; Cobley, C. M.; Chen, J.; Xia, X.; Zhang, Q.; Yang, M.; Cho, E. C.; Brown, P. K. Gold nanocages: from synthesis to theranostic applications. *Acc. Chem. Res.* **2011**, *44*, (10), 914-924.
11. Chen, Y.-S.; Zhao, Y.; Yoon, S. J.; Gambhir, S. S.; Emelianov, S. Miniature gold nanorods for photoacoustic molecular imaging in the second near-infrared optical window. *Nat. Nanotechnol.* **2019**, *14*, (5), 465-472.
12. Liu, Y.; Bhattarai, P.; Dai, Z.; Chen, X. Photothermal therapy and photoacoustic imaging via nanotheranostics in fighting cancer. *Chem. Soc. Rev.* **2019**, *48*, (7), 2053-2108.
13. Akers, W. J.; Kim, C.; Berezin, M.; Guo, K.; Fuhrhop, R.; Lanza, G. M.; Fischer, G. M.; Daltrozzi, E.; Zumbusch, A.; Cai, X. Noninvasive photoacoustic and fluorescence sentinel lymph node identification using dye-loaded perfluorocarbon nanoparticles. *ACS Nano* **2011**, *5*, (1), 173-182.
14. Huang, P.; Lin, J.; Li, W.; Rong, P.; Wang, Z.; Wang, S.; Wang, X.; Sun, X.; Aronova, M.; Niu, G. Biodegradable gold nanovesicles with an ultrastrong plasmonic coupling effect for photoacoustic imaging and photothermal therapy. *Angew. Chem.* **2013**, *125*, (52), 14208-14214.
15. Li, Z.; Yin, S.; Cheng, L.; Yang, K.; Li, Y.; Liu, Z. Magnetic targeting enhanced theranostic strategy based on multimodal imaging for selective ablation of cancer. *Adv. Funct. Mater.* **2014**, *24*, (16), 2312-2321.
16. De La Zerda, A.; Zavaleta, C.; Keren, S.; Vaithilingam, S.; Bodapati, S.; Liu, Z.; Levi, J.; Smith, B. R.; Ma, T.-J.; Oralkan, O. Carbon nanotubes as photoacoustic molecular imaging agents in living mice. *Nat. Nanotechnol.* **2008**, *3*, (9), 557-562.
17. Kim, J.-W.; Galanzha, E. I.; Shashkov, E. V.; Moon, H.-M.; Zharov, V. P. Golden carbon nanotubes as multimodal photoacoustic and photothermal high-contrast molecular agents. *Nat. Nanotechnol.* **2009**, *4*, (10), 688.
18. Liu, Z.; Tabakman, S.; Welsher, K.; Dai, H. Carbon nanotubes in biology and medicine: in vitro and in vivo detection, imaging and drug delivery. *Nano research* **2009**, *2*, (2), 85-120.
19. Song, X.; Gong, H.; Yin, S.; Cheng, L.; Wang, C.; Li, Z.; Li, Y.; Wang, X.; Liu, G.; Liu, Z. Ultra - small iron oxide doped polypyrrole nanoparticles for in vivo multimodal imaging guided photothermal therapy. *Adv. Funct. Mater.* **2014**, *24*, (9), 1194-1201.
20. Pu, K.; Shuhendler, A. J.; Jokerst, J. V.; Mei, J.; Gambhir, S. S.; Bao, Z.; Rao, J. Semiconducting polymer nanoparticles as photoacoustic molecular imaging probes in living mice. *Nat. Nanotechnol.* **2014**, *9*, (3), 233-239.
21. Zhang, Y.; Jeon, M.; Rich, L. J.; Hong, H.; Geng, J.; Zhang, Y.; Shi, S.; Barnhart, T. E.; Alexandridis, P.; Huizinga, J. D. Non-invasive multimodal functional imaging of the intestine with frozen micellar naphthalocyanines. *Nat. Nanotechnol.* **2014**, *9*, (8), 631-638.
22. Jin, Y.; Jia, C.; Huang, S.-W.; O'donnell, M.; Gao, X. Multifunctional nanoparticles as coupled contrast agents. *Nat. Commun.* **2010**, *1*, (1), 1-8.
23. Chen, Y.-S.; Yoon, S. J.; Frey, W.; Dockery, M.; Emelianov, S. Dynamic contrast-enhanced photoacoustic imaging using photothermal stimuli-responsive composite nanomodulators. *Nat. Commun.* **2017**, *8*, (1), 1-10.
24. Huynh, E.; Leung, B. Y.; Helfield, B. L.; Shakiba, M.; Gandier, J.-A.; Jin, C. S.; Master, E. R.; Wilson, B. C.; Goertz, D. E.; Zheng, G. In situ conversion of porphyrin microbubbles to nanoparticles for multimodality imaging. *Nat. Nanotechnol.* **2015**, *10*, (4), 325.
25. Meng, Z.; Zhou, X.; She, J.; Zhang, Y.; Feng, L.; Liu, Z. Ultrasound-responsive conversion of microbubbles to nanoparticles to enable background-free in vivo photoacoustic imaging. *Nano Lett.* **2019**, *19*, (11), 8109-8117.

26. Lu, G. J.; Farhadi, A.; Szablowski, J. O.; Lee-Gosselin, A.; Barnes, S. R.; Lakshmanan, A.; Bourdeau, R. W.; Shapiro, M. G. Acoustically modulated magnetic resonance imaging of gas-filled protein nanostructures. *Nat. Mater.* **2018**, *17*, (5), 456-463.
27. Liu, C.; Zheng, X.; Dai, T.; Wang, H.; Chen, X.; Chen, B.; Sun, T.; Wang, F.; Chu, S.; Rao, J. Reversibly Photoswitching Upconversion Nanoparticles for Super - Sensitive Photoacoustic Molecular Imaging. *Angew. Chem.* **2022**, e202116802.
28. Yin, S.; Li, Z.; Cheng, L.; Wang, C.; Liu, Y.; Chen, Q.; Gong, H.; Guo, L.; Li, Y.; Liu, Z. Magnetic PEGylated Pt 3 Co nanoparticles as a novel MR contrast agent: in vivo MR imaging and long-term toxicity study. *Nanoscale* **2013**, *5*, (24), 12464-12473.
29. Xu, W.; Wang, M.; Li, Z.; Wang, X.; Wang, Y.; Xing, M.; Yin, Y. Chemical transformation of colloidal nanostructures with morphological preservation by surface-protection with capping ligands. *Nano Lett.* **2017**, *17*, (4), 2713-2718.
30. Li, Z.; Jin, J.; Yang, F.; Song, N.; Yin, Y. Coupling magnetic and plasmonic anisotropy in hybrid nanorods for mechanochromic responses. *Nat. Commun.* **2020**, *11*, (1), 1-11.
31. Wang, X.; Feng, J.; Yu, H.; Jin, Y.; Davidson, A.; Li, Z.; Yin, Y. Anisotropically shaped magnetic/plasmonic nanocomposites for information encryption and magnetic-field-direction sensing. *Research* **2018**, 2018, 7527825.
32. Gao, C.; Zhang, Q.; Lu, Z.; Yin, Y. Templated synthesis of metal nanorods in silica nanotubes. *J. Am. Chem. Soc.* **2011**, *133*, (49), 19706-19709.
33. Zhang, J.; Li, Z.; Bai, Y.; Yin, Y. Gold nanocups with multimodal plasmon resonance for quantum-dot random lasing. *Appl. Mater. Today* **2022**, *26*, 101358.
34. Chen, L.; Ji, F.; Xu, Y.; He, L.; Mi, Y.; Bao, F.; Sun, B.; Zhang, X.; Zhang, Q. High-yield seedless synthesis of triangular gold nanoplates through oxidative etching. *Nano Lett.* **2014**, *14*, (12), 7201-7206.
35. Wang, G.; Tao, S.; Liu, Y.; Guo, L.; Qin, G.; Ijiro, K.; Maeda, M.; Yin, Y. High-yield halide-free synthesis of biocompatible Au nanoplates. *Chem. Commun.* **2016**, *52*, (2), 398-401.
36. Liu, X.; Li, B.; Fu, F.; Xu, K.; Zou, R.; Wang, Q.; Zhang, B.; Chen, Z.; Hu, J. Facile synthesis of biocompatible cysteine-coated CuS nanoparticles with high photothermal conversion efficiency for cancer therapy. *Dalton Trans.* **2014**, *43*, (30), 11709-11715.
37. Wang, M.; Gao, C.; He, L.; Lu, Q.; Zhang, J.; Tang, C.; Zorba, S.; Yin, Y. Magnetic tuning of plasmonic excitation of gold nanorods. *J. Am. Chem. Soc.* **2013**, *135*, (41), 15302-15305.
38. Li, Z.; Yin, Y. Stimuli - Responsive Optical Nanomaterials. *Adv. Mater.* **2019**, *31*, (15), 1807061.
39. Feng, J.; Yang, F.; Wang, X.; Lyu, F.; Li, Z.; Yin, Y. Self - aligned anisotropic plasmonic nanostructures. *Adv. Mater.* **2019**, *31*, (19), 1900789.
40. Li, Z.; Yang, F.; Yin, Y. Smart materials by nanoscale magnetic assembly. *Adv. Funct. Mater.* **2020**, *30*, (2), 1903467.
41. Chen, X.; Ye, Z.; Yang, F.; Feng, J.; Li, Z.; Huang, C.; Ke, Q.; Yin, Y. Magnetic cellulose microcrystals with tunable magneto-optical responses. *Appl. Mater. Today* **2020**, *20*, 100749.
42. Chen, Q.; Xu, L.; Chen, J.; Yang, Z.; Liang, C.; Yang, Y.; Liu, Z. Tumor vasculature normalization by orally fed erlotinib to modulate the tumor microenvironment for enhanced cancer nanomedicine and immunotherapy. *Biomaterials* **2017**, *148*, 69-80.
43. Yao, J.; Wang, L. V. Sensitivity of photoacoustic microscopy. *Photoacoustics* **2014**, *2*, (2), 87-101.
44. Wang, S.; Lin, J.; Wang, T.; Chen, X.; Huang, P. Recent advances in photoacoustic imaging for deep-tissue biomedical applications. *Theranostics* **2016**, *6*, (13), 2394.
45. Mallidi, S.; Luke, G. P.; Emelianov, S. Photoacoustic imaging in cancer detection, diagnosis, and treatment guidance. *Trends Biotechnol.* **2011**, *29*, (5), 213-221.

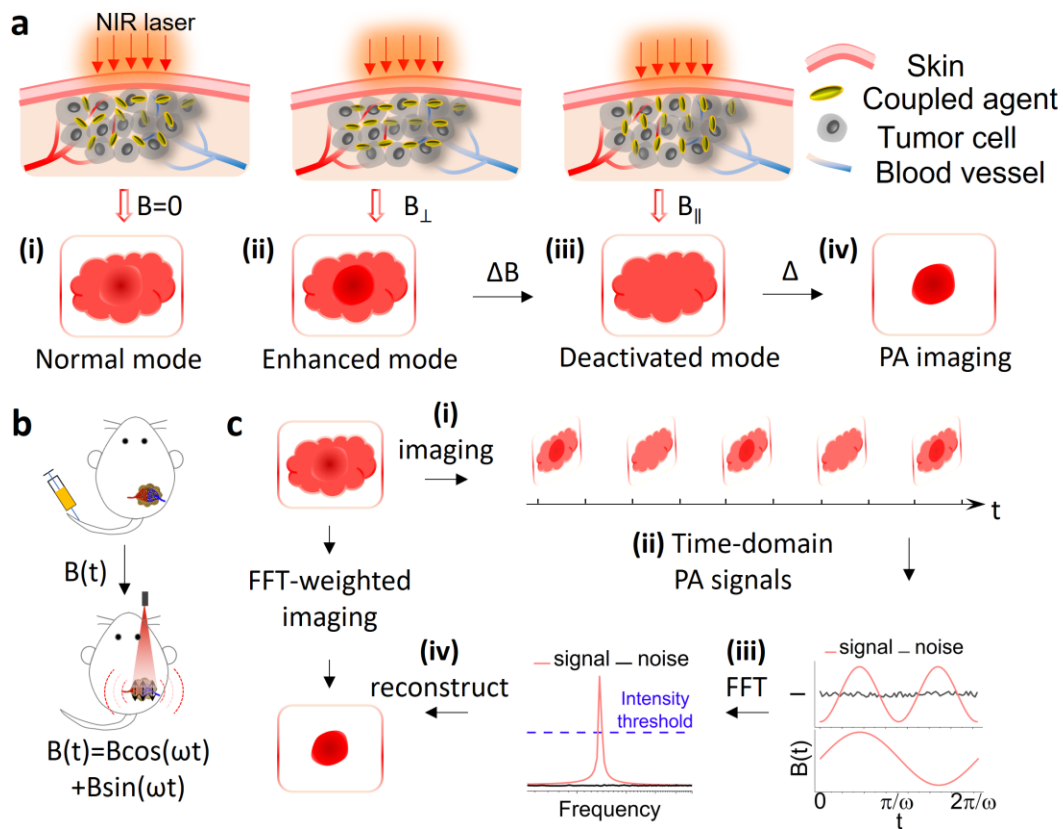


Figure 1. Working mechanism and data processing of the background-free PA imaging. (a) Schematic illustration of the background-free PA imaging through pixel-wise subtraction using $\text{Fe}_3\text{O}_4@\text{Au}$ nanorods as active contrast agents. Normal PA mode (i) is produced in the absence of a magnetic field, and the enhanced PA mode (ii) and deactivated PA mode (iii) are realized under perpendicular and parallel magnetic fields, respectively. (b) Schematic illustration of the magnetically modulated, FFT-weighted PA imaging under an alternating magnetic field. (c) Schematic illustration of the imaging method and data processing. In (i), time-series images are acquired under the alternating magnetic field. In (ii), the PA signals from each pixel are extracted and plotted in the time domain. In (iii), FFT is introduced to transform the PA signals in the time domain into intensity in the frequency domain. The periodic and dynamic PA signals of smart contrast agents can be distinguished from the random PA signals of background noises and screened across the whole imaging domain. In (iv), an FFT-weighted image can be reconstructed using the intensity of PA signals in the frequency domain.

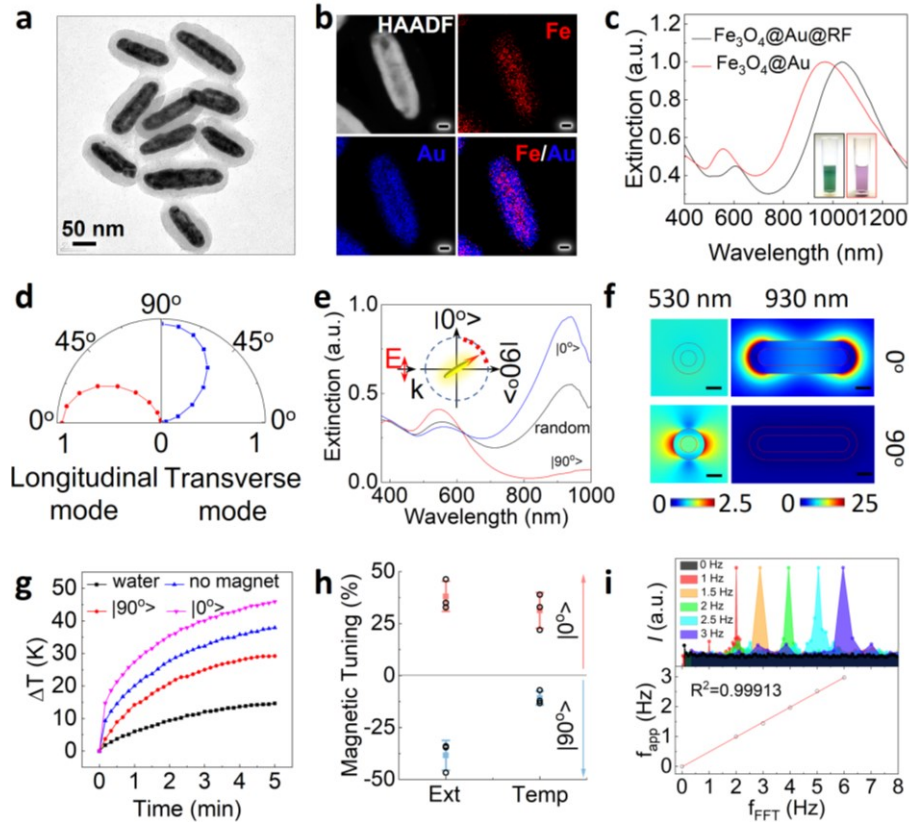


Figure 2. Magnetic modulation of the physical properties of $\text{Fe}_3\text{O}_4@Au$ NRs. (a) TEM images of $\text{Fe}_3\text{O}_4@Au@RF$ NRs. (b) HAADF imaging and elemental mapping of the $\text{Fe}_3\text{O}_4@Au@RF$ NRs. Scale bars: 10 nm. (c) Extinction spectra of $\text{Fe}_3\text{O}_4@Au@RF$ NRs before and after removing RF shells. Insets: pictures of colloidal dispersions of the $\text{Fe}_3\text{O}_4@Au@RF$ NRs (left panel) and $\text{Fe}_3\text{O}_4@Au$ NRs (right panel). (d) Dependence of the transverse and longitudinal plasmonic excitation on nanorod orientation. (e) Extinction spectra of nanorod dispersion under different magnetic fields, with the measurement geometry shown in the inset. (f) Electric field distribution of orientated nanorods under light excitation at resonant wavelength. Scale bars: 20 nm. (g) Temperature change of a nanorod dispersion illuminated by 980-nm light. A magnetic field was used to control the nanorod orientation. (h) Tunability of optical extinction and temperature under different magnetic fields. (i) FFT of magnetically modulated PA signals (top panel) and the correlation between FFT frequency and applied magnetic field frequency (bottom panel).

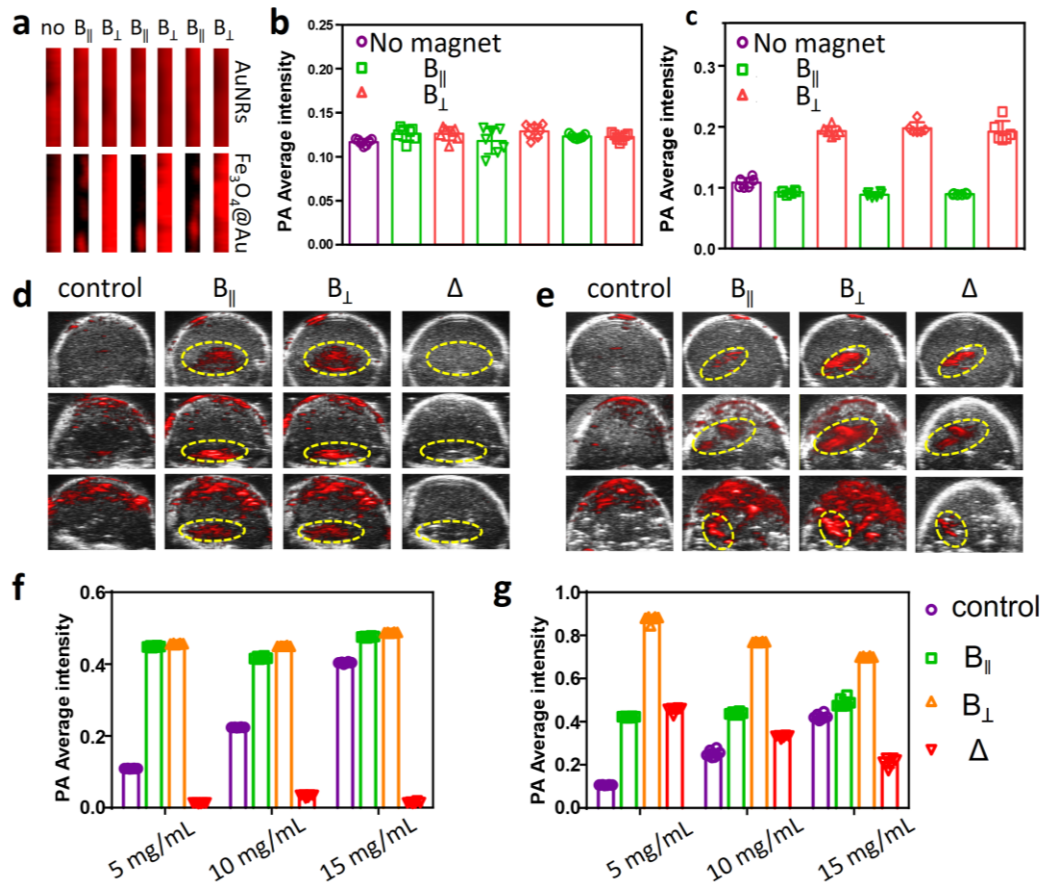


Figure 3. Actively modulating PA signals using external magnetic fields. (a) PA imaging of AuNRs (top panel) and $Fe_3O_4@Au$ NRs (bottom panel) under magnetic fields of different orientations. The field strength is 0.4 T. (b-c) the corresponding PA signal intensity of AuNRs (b) and $Fe_3O_4@Au$ NRs (c). Active modulation of PA signals using PDA phantoms. (d-e) PA images of PDA phantoms with AuNRs (d) and $Fe_3O_4@Au$ NRs (e). The concentrations of PDA in the gel are 5 mg/mL, 10 mg/mL, and 15 mg/mL in the top, middle, and bottom panels, respectively. (f-g) the average PA signals of AuNRs (f) and $Fe_3O_4@Au$ NRs (g) under different magnetic fields. The wavelength of incident light in PA imaging is 910 nm.

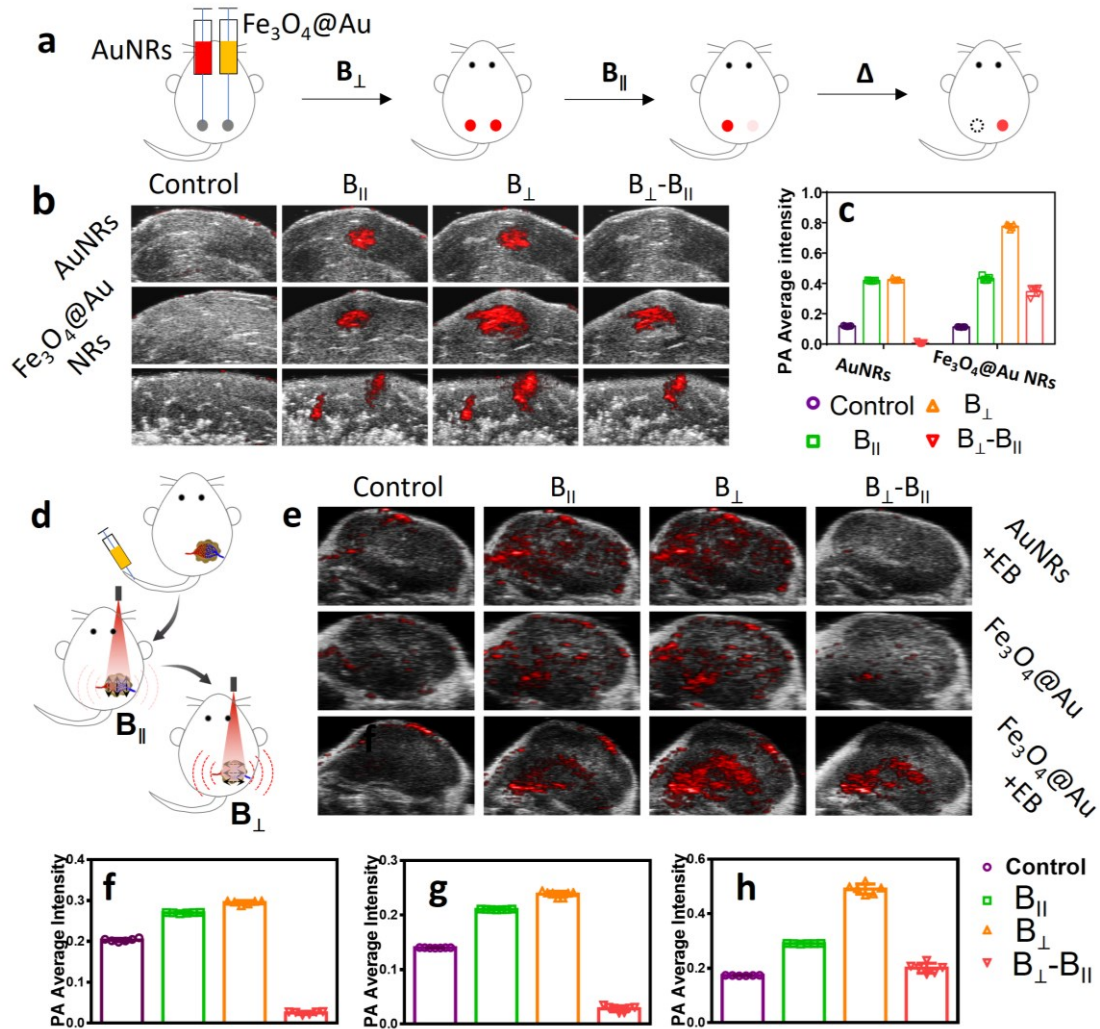


Figure 4. Active modulation of PA signals by *in vivo* nanoscale magnetic alignment of $\text{Fe}_3\text{O}_4@Au$ NRs. (a) Working principle of background-free PA imaging based on *in vivo* nanoscale magnetic alignment of $\text{Fe}_3\text{O}_4@Au$ NRs and pixel subtraction. (b) PA imaging of mouse muscles after injecting AuNRs and $\text{Fe}_3\text{O}_4@Au$ NRs. In the bottom panel, the AuNRs and $\text{Fe}_3\text{O}_4@Au$ NRs were injected into the left and right sites, respectively. (c) PA signal changes mediated by magnetic fields with varying directions. The field strength is 0.4 T. (d) Schematic illustration of the background-free PA imaging of tumor using intravenous (i.v.) injection of $\text{Fe}_3\text{O}_4@Au$ NRs. (e) PA imaging after i.v. injection of AuNRs and $\text{Fe}_3\text{O}_4@Au$ NRs. (f-h) The signal changes of PA imaging before and after data processing for tumors treated with AuNRs (f), $\text{Fe}_3\text{O}_4@Au$ NRs (g), and treated with $\text{Fe}_3\text{O}_4@Au$ NRs and erlotinib (h). Background-free imaging ($B_{\perp}-B_{\parallel}$) is processed by subtracting the PA image pixels measured under a perpendicular magnetic field (B_{\perp}) from those measured under a parallel field (B_{\parallel}).

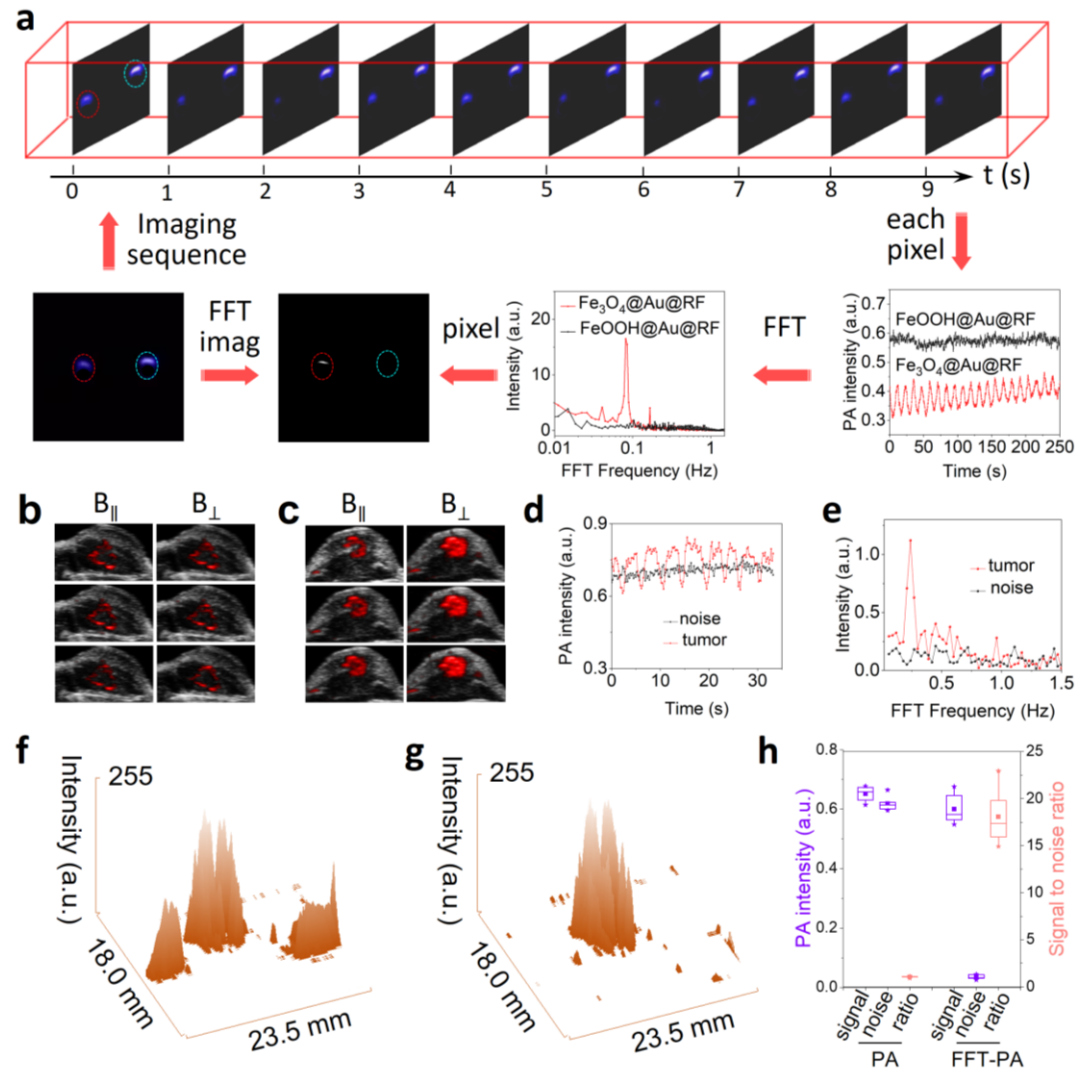


Figure 5. FFT-weighted background-free PA imaging. (a) Data processing of the magnetically modulated, FFT-weighted background-free PA imaging. (b-c) PA imaging of tumors after injection of AuNRs (b) and $\text{Fe}_3\text{O}_4@Au$ NRs (c) under magnetic fields in two different directions. Magnetic fields parallel and perpendicular to light incidence direction are denoted as B_{\parallel} and B_{\perp} , respectively. (d) Real-time PA signals of two representative pixels in tumors and backgrounds under an alternating magnetic field with a frequency of 0.125 Hz. (e) FFT of the PA signals of $\text{Fe}_3\text{O}_4@Au$ NRs and the background noises under the alternating magnetic field. (f-g) the signals of conventional (f) and FFT-weighted, background-free PA imaging (g). (h) Summary of PA intensity of tumors and the background and signal-to-noise ratio in conventional PA and FFT-weighted PA (FFT-PA) imaging.

TOC Graphic:

